Descending pathway facilitates undulatory wave propagation in *Caenorhabditis elegans* through gap junctions

Tianqi Xu[a,b,1], Jing Huo[a,b,1], Shuai Shao[a,b], Michelle Po[c,d,e], Taizo Kawano[c,d,e], Yangning Lu[c,d,e], Min Wu[c,d,e], Mei Zhen[c,d,e], and Quan Wen[a,b,f,2]

[a]Hefei National Laboratory for Physical Sciences at the Microscale, School of Life Sciences, University of Science and Technology of China, 230027 Hefei, China; [b]Chinese Academy of Sciences Key Laboratory of Brain Function and Disease, 230027 Hefei, China; [c]Lunenfeld–Tanenbaum Research Institute, Mount Sinai Hospital, University of Toronto, Toronto, ON M5G 1X5, Canada; [d]Department of Molecular Genetics, University of Toronto, Toronto, ON M5G 1X5, Canada; [e]Department of Physiology, University of Toronto, Toronto, ON M5G 1X5, Canada; and [f]Center for Excellence in Brain Science and Intelligence Technology, Chinese Academy of Sciences, Shanghai 200031, China

Edited by Paul W. Sternberg, California Institute of Technology, Pasadena, CA, and approved March 22, 2018 (received for review September 29, 2017)

Descending signals from the brain play critical roles in controlling and modulating locomotion kinematics. In the *Caenorhabditis elegans* nervous system, descending AVB premotor interneurons exclusively form gap junctions with the B-type motor neurons that execute forward locomotion. We combined genetic analysis, optogenetic manipulation, calcium imaging, and computational modeling to elucidate the function of AVB-B gap junctions during forward locomotion. First, we found that some B-type motor neurons generate rhythmic activity, constituting distributed oscillators. Second, AVB premotor interneurons use their electric inputs to drive bifurcation of B-type motor neuron dynamics, triggering their transition from stationary to oscillatory activity. Third, proprioceptive couplings between neighboring B-type motor neurons entrain the frequency of body oscillators, forcing coherent bending wave propagation. Despite substantial anatomical differences between the motor circuits of *C. elegans* and higher model organisms, converging principles govern coordinated locomotion.

descending pathway | motor control | central pattern generator | *C. elegans* | proprioception

Locomotion requires coordinated rhythmic motor activity. In both vertebrate and invertebrate motor systems, oscillatory signals that innervate muscles are generated by dedicated neurons and neural circuits with intrinsic rhythmic properties, called the central pattern generators (CPGs) (1–6). Movements, which constitute muscle activities of defined spatial pattern and temporal sequence, are driven by oscillators distributed at different body segments. Coordination of rhythmic movements requires coupling mechanisms, by which the rhythm of multiple CPGs becomes frequency- and phase-locked (5, 7).

Although the oscillatory activity of CPGs can be maintained independently of sensory inputs, proprioceptive or mechanosensitive feedbacks reshape motor dynamics during movements (8). In lamprey and leech, for example, activation of specialized proprioceptive neurons, either by current injection or imposed body bending, entrains the motor CPG activity (9, 10). In limbed animals, rapid phasic feedback from mechanoreceptors tunes the rhythmic firing of motor neurons during step cycles (11–13). Mice lacking Piezo2, a mechanically activated channel expressed in proprioceptive neurons, exhibit severely uncoordinated body movement (14).

Descending signals, typically the projections of glutamatergic interneurons from the brain to the spinal or nerve cords, regulate both spinal CPG activities and motor patterns (15). In fish and rodent, descending reticulospinal neurons, arising from the brainstem and innervating excitatory spinal interneurons, can initiate locomotion and modulate speed (16–19), whereas those that activate inhibitory spinal interneurons can terminate locomotion (20). Descending interneurons that directly target the forelimb motor neurons are critical for skillful motor behaviors (21). In leech, activation of a descending command interneuron, cell 204, can initiate and maintain swimming (7, 22).

A deep understanding of the motor circuit must integrate local CPG elements, sensory feedback, and global command signals, to predict behavioral dynamics that result from the interaction of individual circuit components (23, 24). With a connectome at synaptic resolution and fully identified cell types (25, 26), *Caenorhabditis elegans* offers an opportunity to obtain a system-level understanding of a locomotor circuit.

The *C. elegans* ventral nerve cord consists of a network of excitatory cholinergic motor neurons, including the A and B types that execute backward and forward movement, respectively, and the inhibitory motor neurons (D type) that are innervated by the excitatory motor neurons (27). The AVB premotor interneurons, which receive inputs from many sensory neurons and interneurons, extend processes along the entire ventral nerve cord and exclusively form gap junctions with the B-type motor neurons (26, 28, 29) (illustrated in Fig. 1*A*). The AVB premotor interneurons are required for forward locomotion (30); the precise function of their electrical synapses with B-type motor neurons, however, is not well understood.

Significance

A deep understanding of the neural basis of motor behaviors must integrate neuromuscular dynamics, mechanosensory feedback, as well as global command signals, to predict behavioral dynamics. Here, we report on an integrative approach to define the circuit logic underlying locomotion in *Caenorhabditis elegans*. Our combined experimental and computational analyses revealed that (*i*) motor neurons in *C. elegans* function as oscillators; (*ii*) descending interneuron inputs and proprioceptive coupling between motor neurons work synergistically to facilitate the sequential activation of motor neuron activities, allowing bending waves to propagate efficiently along the body. Our work represents a key step toward an integrative view of animal locomotion.

Author contributions: T.X. and Q.W. designed research; T.X., J.H., S.S., and Q.W. performed research; T.X., J.H., M.P., T.K., Y.L., M.W., and M.Z. contributed new reagents/analytic tools; T.X., J.H., S.S., and Q.W. analyzed data; and T.X., S.S., M.Z., and Q.W. wrote the paper.

The authors declare no conflict of interest.

This article is a PNAS Direct Submission.

[1]T.X. and J.H. contributed equally to this work.

[2]To whom correspondence should be addressed. Email: qwen@ustc.edu.cn.

This article contains supporting information online at www.pnas.org/lookup/suppl/doi:10.1073/pnas.1717022115/-/DCSupplemental.

Published online April 23, 2018.

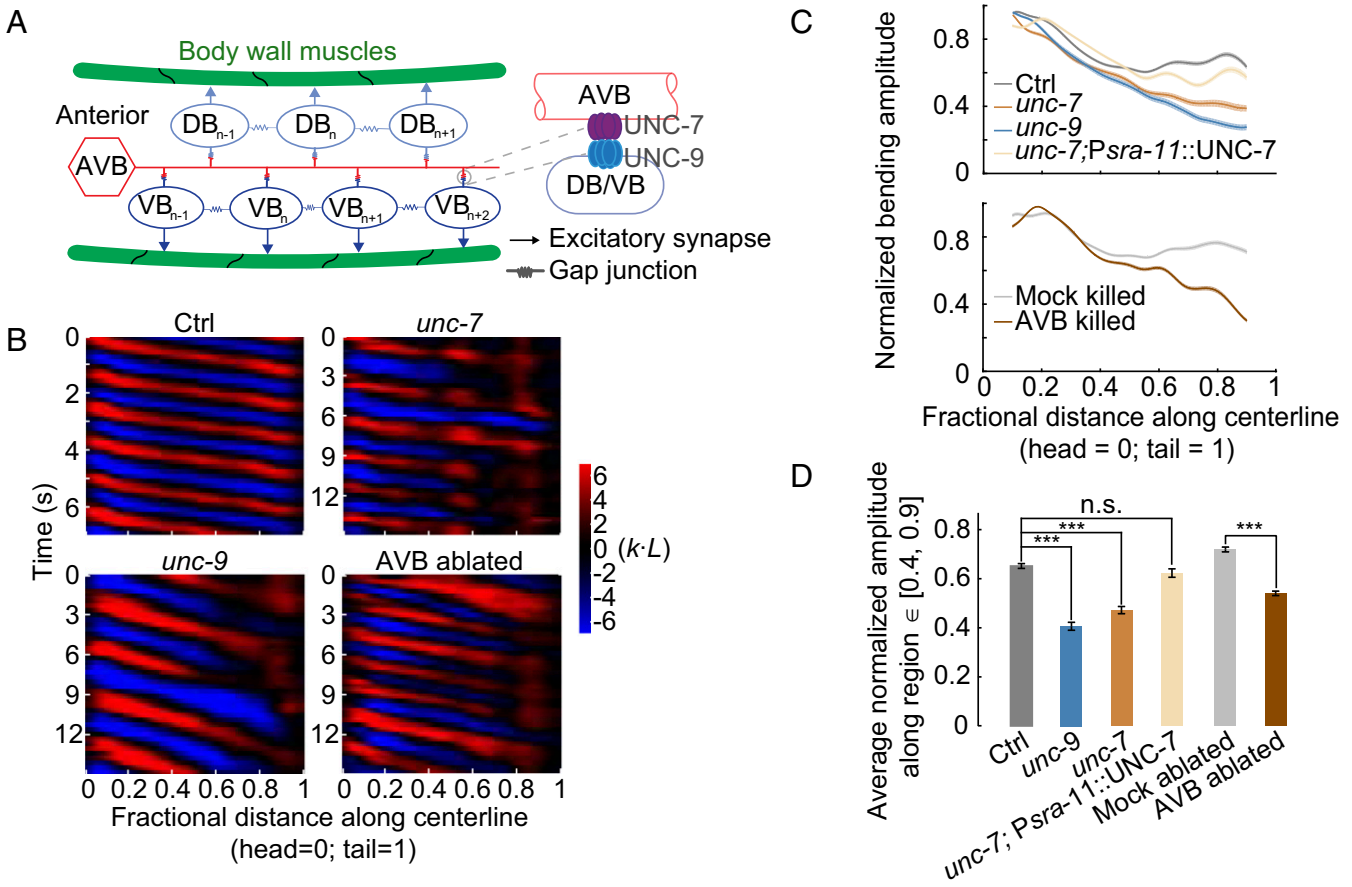

Fig. 1. AVB-B gap junctions facilitate undulatory wave propagation during forward locomotion. (*A*) Schematics of gap junction couplings in the *C. elegans* forward motor circuit. The AVB premotor interneurons form gap junctions with all B-type motor neurons, which drive dorsal (DB) and ventral (VB) muscle contraction. AVB-B gap junctions require the expression of innexin UNC-7 in AVB interneurons and UNC-9 in B-type motor neurons. Neighboring B-type neurons are also gap junction coupled. Other types of motor neurons have been omitted from the diagram for simplicity. (*B*) Representative curvature kymographs of control [N2; P*unc-4*::TWK-18(gf)], *unc-7* [*unc-7*(*hp121*); P*unc-4*::TWK-18(gf)], *unc-9* [*unc-9*(*fc16*); P*unc-4*::TWK-18(gf)] animals, and AVB-ablated [P*lgc-55(B)*::miniSOG; P*unc*-4::TWK-18(gf)] and their control (Mock-ablated) animals. Worms swam in viscous solutions (~1 Pa·s viscosity). Body curvature was defined as a nondimensional unit *k*·*L*, where *L* is the body length. (*C*) Quantification of the bending amplitude along the body for strains described above. Shaded regions represent SEM. Amplitude was normalized against the maximum curvature along the body. (*D*) Averaged bending amplitude in the posterior body ∈ [40, 90] for strains described above. ***$P < 0.0001$, two-sample *t* test with Bonferroni correction; n.s., $P = 0.16$. Error bars represent SEM. Ctrl, n = 105 measurements, 13 worms; *unc-7* mutant, n = 149 measurements, 22 worms; *unc-9* mutant, n = 93 measurements, 17 worms; AVB-ablated, n = 80 measurements, 13 worms; Mock (same genotype without ablation), n = 96 measurements, 12 worms.

We undertook an integrative approach to address the circuit logic underlying forward locomotion in *C. elegans*, with an emphasis on how descending signals modulate the motor circuit dynamics. Descending inputs in other systems have been implicated in driving or modulating the activity of locomotor CPGs (16–18). Combining molecular genetics, optical manipulation of neuronal activity, and calcium imaging, we demonstrated that midbody B-type motor neurons could function as oscillators. AVB-B gap junctions drive the bifurcation of the B-type neuron dynamics from stationary to rhythmic activity, which promotes body bending during forward movement.

To generate coherent body undulation, motor neuron activities were entrained by proprioceptive feedback. Previously, we demonstrated the proprioceptive property of the B-type motor neurons in the mid and posterior body segments; such a property supports proprioceptive coupling between these B-type motor neurons and contributes to directional propagation of rhythmic body bending (31, 32). Combining experimental and computational analyses, we suggest that descending signals from AVB function synergistically with proprioceptive couplings to facilitate sequential activation of B-type motor neurons, allowing body bending to propagate directionally and efficiently to drive forward locomotion.

Results

Gap Junctions Between AVB Premotor Interneurons and B-Type Motor Neurons Facilitate Bending Wave Propagation During Forward Locomotion. The AVB premotor interneurons and B-type motor neurons form heterotypic gap junctions via the UNC-7 innexin (in AVB) and UNC-9 innexin (in B-type motor neurons) (Fig. 1*A*) (28, 29). To determine whether AVB-B gap junctions play a role in forward locomotion, we first examined the motor behaviors of *unc-7*(*hp121*) and *unc-9*(*fc16*) null mutants immersed in viscous solution (1 Pa·s viscosity). In these gap junction-deficient mutants, the intrinsically higher levels of activity in the A-type motor neurons, which control backward locomotion, prevent animals from generating continuous forward movement (29). To reduce interference from motor activity arising from the backward motor circuit, A-type motor neurons were constitutively silenced by an ectopically expressed K^+ channel [P*unc-4*::TWK-18(gf)] (29) in examined strains (Table S1) and subsequent experiments.

We visualized and quantified *C. elegans* locomotion kinematics by curvature kymographs (Fig. 1*B*). During bouts of forward movement, each body segment alternated between positive (red)

and negative (blue) curvature, and the stripes of curvature propagated from the head to the tail. Coordinates along the worm body were defined as head = 0 and tail = 1 (Fig. 1*B*). In control animals (wild type with A-type motor neurons constitutively silenced), the bending amplitude was highest near the head, and then declined gradually and plateaued at the midbody (~40% of the body length, Fig. 1*C*). Both *unc-7* and *unc-9* mutants exhibited identical phenotypes: their bending amplitudes diminished monotonically from the head toward the tail (Fig. 1 *B* and *D* and Movie S1).

UNC-7 and UNC-9 are expressed by many neurons besides the AVB and B-type neurons (28, 33). We found that the disruption of AVB-B gap junctions was responsible for the monotonic decline of forward-driving bending amplitudes in *unc-7* and *unc-9* mutants. First, when AVB premotor interneurons were optogenetically ablated using a mini-singlet oxygen generator (miniSOG) (34) [by either P*lgc-55(B)*::TOMM20-miniSOG or P*sra-11*::PH-miniSOG], we observed the same trend of bending amplitude decline toward the tail (Fig. 1 *B* and *D* and Fig. S1). Second, restoring innexin UNC-7 in AVB (*unc*-7; P*sra-11*::UNC-7) in *unc-7* mutants was sufficient to restore the plateau phase of bending amplitude (Fig. 1 *C* and *D* and Movie S3). We also noticed that the frequency of undulatory waves (Fig. 1*B* and Fig. S1*A*) was significantly reduced in *unc-7*, *unc-9* mutants, and AVB-ablated animals. The current study focused on bending amplitude propagation.

Linear Model Predicts Deteriorated Undulatory Wave in the Presence of AVB-B Gap Junctions. How do AVB-B gap junctions promote efficient body bending propagation toward the tail? Previously, we showed that worm undulation during forward locomotion involves local and directional proprioceptive coupling between adjacent body regions (31). Curvature change in a midbody region, induced by a pneumatic microfluidic device, activates bend-sensitive B-type neurons and defines the curvature of the posterior neighbor (31). Consistently, when we trapped the middle body region of a wild-type worm in a static channel with defined curvature, the unrestrained posterior body region exhibited bending curvature in the same direction as that imposed by the microfluidic channel (Fig. 2 *A* and *B* and ref. 31).

A simple possibility is that proprioceptive coupling is UNC-7- and UNC-9–dependent. To test this possibility, we examined *unc-7* and *unc-9* mutants constrained by microfluidic channels. Consistent with a previous finding (31) and as observed for control animals, their posterior body regions still followed the curvature imposed on the anterior regions (Fig. 2 *B* and *C* and Fig. S2). Therefore, proprioceptive coupling remains largely intact in the absence of UNC-7– or UNC-9–dependent gap junctions.

We next took a theoretic approach to probe how AVB-B gap junctions might affect bending wave propagation. We first adopted a linear model (31), where we asserted that undulatory waves start with rhythmic dorsal–ventral alternative bends near the head; directional proprioceptive coupling between adjacent body regions is fully described by the following first-order differential equations:

$$\begin{cases} C_m\dfrac{dv_i}{dt} = g_m(-v_i + ck_{i-1}) - g(v_i - v_{AVB}) \\ \tau_h\dfrac{du_i}{dt} = -u_i + v_i \qquad i = 2,\ 3,\ \ldots 6. \\ \tau_\eta\dfrac{dk_i}{dt} = -k_i + \alpha_{\max} * u_i/b \end{cases} \quad [1]$$

We divided the worm into six segments, with subscript i as the segment number. In the first equation, v describes relative motor neuron activity: when dorsal B-type neurons have a higher activity than ventral ones, $v > 0$, and vice versa. k_i is the curvature of a given segment, and ck_{i-1} describes the proprioceptive signal from the neighboring anterior body segment, where $c > 0$ is the coupling strength. C_m is the membrane capacitance and g_m the leaky conductance. The term $-g(v_i - v_{AVB})$ describes the contribution from AVB-B electrical coupling, where g is the gap junction conductance. Here, we set AVB membrane potential at a constant depolarized value, which is consistent with experimental observations that AVB exhibit elevated yet nonoscillatory calcium activity during forward locomotion (29, 35, 36). In Eq. **1**, for simplicity, we set $v_{AVB} = 0$ to eliminate the bias of v. A more detailed model that treats dorsal and ventral motor neuron activities separately is described in *Supporting Information*.

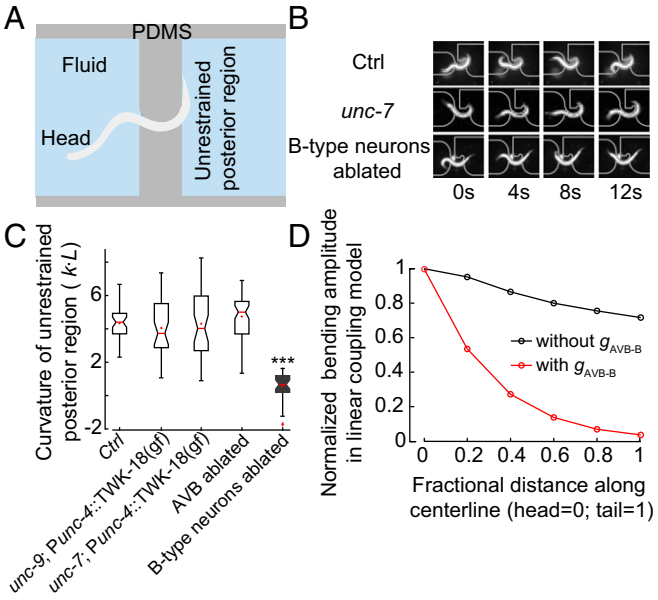

Fig. 2. UNC-7– and UNC-9–dependent gap junctions are not required for proprioceptive couplings in the forward motor circuit. (*A*) Schematics of the microfluidic device for constraining a body segment with defined curvature. (*B*) Time-lapse video images of control (*Upper*), *unc-7* (*Middle*), and B-type neurons ablated (*Lower*) worms trapped in the microfluidic device. In both control and *unc-7* mutant animals, the posterior unrestrained body region followed the curvature of the channel. However, this was not the case when B-type motor neurons were optogenetically ablated. (*C*) In AVB-B gap junction-deficient mutants, or AVB-ablated worms, the posterior unrestrained body region also followed the curvature of the channel. Boxes indicate Q1 to Q3, error bars represent Q1 − 1.5IQR and Q3 + 1.5IQR, respectively, and notches indicate 95% confidence interval. ***$P < 0.0001$, compared with other strains, by Mann–Whitney *U* test. Control [N2; P*unc-4*::TWK-18(*gf*)], $n = 40$ measurements, 8 worms; *unc-7* [*unc-7*; P*unc-4*::TWK-18(gf)], $n = 41$ measurements, 12 worms; *unc-9* [*unc-9*; P*unc-4*::TWK-18(gf)], $n = 38$ measurements, 9 worms; AVB-ablated [P*lgc-55(B)*::miniSOG], $n = 60$ measurements, 10 worms; B-ablated (P*acr-5*::miniSOG), $n = 33$ measurements, 9 worms. (*D*) In the linear model, incorporating the AVB-B gap junction inputs further deteriorated bending wave propagation.

The second equation relates motor neuron activity to muscle torque: u is a dimensionless variable and $\alpha_{\max} * u$ is the maximum torque that the muscle cells can generate. The last equation describes how the segment curvature changes with muscle torque: b is the bending modulus of the body and τ_η is a time constant (31). Published work (31, 37, 38) has established that when *C. elegans* swam in viscous solution (our experimental condition), the biomechanics of the worm body can be modeled as elastic rod bent in viscous medium at low Reynolds number, and the inertia can be ignored. If we consider sinusoidal dynamics of curvature and torque, the time constant τ_η has the following expression (31, 37):

$$\tau_\eta = \frac{C_N}{b}\left(\frac{2\pi}{\lambda}\right)^4 \approx \frac{30\eta}{b}\left(\frac{2\pi}{\lambda}\right)^4, \quad [2]$$

where C_N is the drag coefficient perpendicular to the worm body, a parameter that is proportional to the viscosity of medium η, and λ is the spatial wavelength of undulation.

Simulation of the linear model predicted an exponential decay of bending amplitude toward the tail (Fig. 2*D*). By considering a continuous form of local coupling (*Supporting Information*), we solved the linear model analytically and identified a self-consistent solution for the spatiotemporal profile of the body curvature:

$$k(x,t) = k_0 \exp(-x/\xi)\exp\left(i\left(\frac{2\pi x}{\lambda} - \omega t + \phi(x)\right)\right), \qquad [3]$$

where ω describes the angular frequency; $\phi(x)$ is a phase lag term, and ξ is the decay length constant, which, to the leading order, is given by the following:

$$\xi \approx \frac{l}{1 - c\alpha_{\max}/b}, \quad \text{subject to} \quad \frac{c\alpha_{\max}}{b} \leq 1, \qquad [4]$$

where l is the spatial scale for local proprioceptive coupling (31). $\xi \to +\infty$ leads to identical bending amplitude along the body. Incorporation of AVB-B electrical coupling effectively changes c to $cg_m/(g_m + g)$. This prefactor further reduces the length constant.

Therefore, in a linear coupling model where the B-type motor neurons are passive recipients of proprioceptive inputs, opposite to our experimental findings, gap junctions between AVB and B-type neurons would further deteriorate the bending wave propagation (Fig. 2*D*).

B-Type Motor Neurons Are Nonlinear Functional Units. The discrepancy between the theoretical model and experimental observations indicates that some basic assumption in the linear model must be modified. We hypothesized that proprioceptive signals may couple nonlinear functional units within adjacent regions. Oscillation is a common form of nonlinearity. We thus tested whether CPGs exist along the worm nerve cord.

Our linear coupling model predicted that abolishing head bending activity would abolish the undulatory wave; a coupled-CPG model (39), however, predicts the opposite. To distinguish these possibilities, we performed selective optogenetic inhibition of B-type motor neurons in a defined anterior body region (0.1–0.3 along worm coordinates) of a freely swimming animal (P*acr-5*::Arch) (Fig. 3 *A* and *B* and Movie S2). Upon green light illumination, we effectively abolished bending near the head region (Fig. 3*B*, curvature kymograph). In the absence of local proprioceptive signal from adjacent anterior body region, the midbody (~50% of the body length), however, continued to generate rhythmic bending with increased undulation frequency and reduced amplitude (Fig. 3 *B* and *E* and Movie S2). When a worm swam in 1 Pa·s viscous solution, the undulation frequency was ~0.8 Hz (Fig. 3*C*); when anterior bending activity was optogenetically inhibited, the midbody undulation frequency doubled (~1.6 Hz, Fig. 3*C*). We observed a similar phenomenon when anterior undulation was abolished optogenetically, either by inhibiting both the A-type and B-type motor neurons (P*acr-2*::Arch, Fig. S3*A*), or by directly inhibiting anterior muscle cells (P*myo-3*::NpHR, Fig. S3*A*).

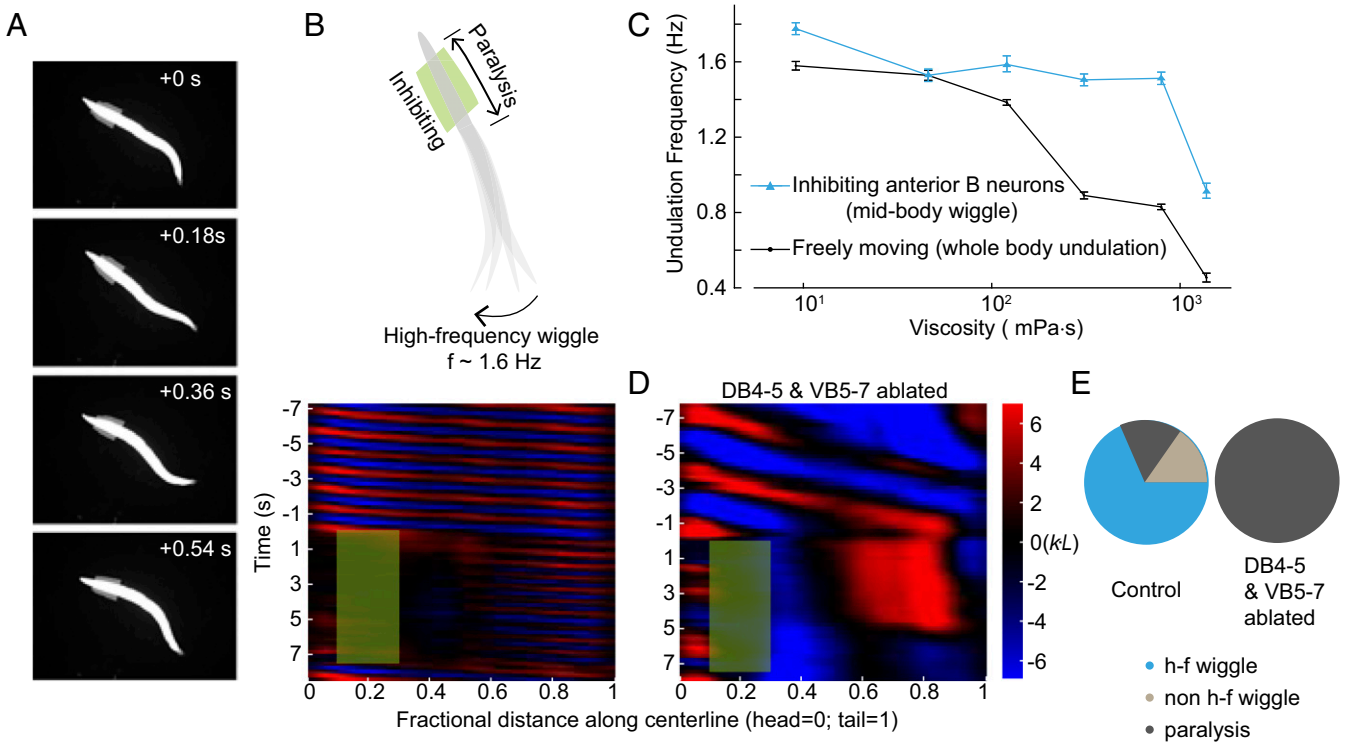

Fig. 3. Midbody B-type motor neurons generate rhythmic activity independent of proprioceptive coupling. (*A*) Time-lapse video images from a recording when B-type motor neurons in an anterior body region (10–30% along the worm body) were optogenetically inhibited. (*B, Upper*) Schematic illustrates the effect of spatially selective inhibition of B-type motor neurons. Optogenetic inhibition of anterior B-type motor neurons induced high-frequency undulation in the posterior region. (*Lower*) Representative curvature kymograph. Green shaded region shows the selected spatiotemporal region for optogenetic inhibition. (*C*) *C. elegans* undulation frequency at different viscosity. Black line is undulation frequency of control animals; blue line is midbody undulation frequency when anterior bending activity was abolished. Error bars are SEM; $n \geq 8$ worms for each data point. (*D*) Representative curvature kymograph during optogenetic inhibition of anterior B-type motor neurons, with and without midbody B-type neurons (DB 4–5 and VB 5–7). (*E*) Pie chart summarizes the percentage of locomotor states when anterior bending activity was abolished. h-f wiggle: midbody undulation frequency was higher than that before anterior bending activity was abolished; non–h-f wiggle: midbody undulation frequency was equal to or less than that before anterior bending activity was abolished; paralysis: no waves emerged in the midbody. Control (P*acr-5*::Arch), n = 241 measurements, 20 worms; midbody B-type neuron-ablated worms (P*acr-5*::Arch; P*acr-5*::miniSOG), n = 77 measurements, 11 worms.

These observations favor the possibility that at least some B-type motor neurons are intrinsic oscillators. Whereas the normal undulation frequency decreased in more viscous solution (Fig. 3*C* and ref. 37), the midbody undulation frequency remained fixed across a wide range of viscosities (<1 Pa·s) when anterior bending activity was abolished (Fig. 3*C* and Fig. S3*B*). The frequency of the midbody oscillators, which could be entrained by head bending, appeared to only weakly depend on the mechanical load of the environment.

To determine whether the B-type motor neurons were responsible for generating midbody oscillation, we performed systematic ablation of B-type neurons (P*acr-5*::miniSOG) in the ventral nerve cord. Ablating a cluster of midbody B-type motor neurons (DB4-5 and VB5-7) abolished high-frequency oscillation when anterior bending activity was abolished (Fig. 3 *D* and *E*). When only a subset of neurons in this cluster was ablated, the high-frequency midbody undulation could still be induced (Fig. S3*A*). In these animals, we occasionally observed independent bending waves generated by the head and posterior body regions, respectively (Fig. S3*C*). When the activity of other ventral cord motor neurons was blocked, either by silencing the A-type motor neurons (P*unc*-4::TWK-18, Fig. 4*B*, control) or by eliminating inhibitory neurotransmitter release (Fig. S3*A*), B-motor neuron-dependent midbody undulation persisted. These data, together with the observation that the midbody undulated in the absence of proprioceptive signal arising from the adjacent anterior region (Fig. 3*B* and Fig. S3*A*), strongly suggest that these B-type motor neurons do not passively respond to proprioceptive signals. They instead function as nonlinear units that resemble CPG modules distributed along the body.

AVB-B Gap Junctions Drive Bifurcation of B-Type Motor Neuron Dynamics. We next asked whether AVB-B gap junctions play a role in high-frequency midbody undulation when the anterior bending activity is abolished. In AVB-B gap junction-deficient mutants (*unc-7* and *unc-9*), as well as AVB-ablated animals, optogenetic inhibition of anterior bending no longer induced midbody undulation (Fig. 4 *A* and *B*). Instead, optogenetic inhibition of either the anterior B-type motor neurons, or anterior body wall muscles led to paralysis of the entire body (Fig. 4 *A* and *B* and Fig. S4). Restoring UNC-7 innexin expression in several interneurons including AVB (*unc*-7; P*sra-11*::UNC-7) significantly increased the efficacy for inducing high-frequency midbody undulation (Fig. 4*B* and Movie S3). These results suggest that AVB interneurons and their gap junction couplings with the B-type motor neurons are required for inducing midbody high-frequency undulation. Consistently, optogenetic activation of several interneurons that include AVB (*Psra-11*::Chrimson) triggered forward locomotion from either the pause state or the backward movement (Fig. 4*C* and Movie S7), whereas their optogenetic inhibition (P*sra-11*::GtACR2) (40) reliably halted forward locomotion (Fig. 4*D* and Movie S8).

To directly investigate whether B-type motor neurons could generate rhythmic activities in the presence of AVB gap junction inputs, we performed calcium imaging of B-type motor neurons in *unc-13(e51)*, a mutation that largely eliminates chemical synaptic transmission of all neurons, whereas the electrical synapses persist. In the absence of AVB activation (control in Fig. S4), B-type motor neurons did not exhibit rhythmic calcium activities. Upon optogenetic activation of AVB (P*sra-11*::Chrimson), B-type motor neurons in the midbody region exhibited rhythmic calcium activities (Fig. 4 *E* and *F* and Fig. S4).

Given that AVB calcium activities are nonoscillatory (29, 35, 36), our data suggest that AVB-B gap junctions drive bifurcation of B-type neuron dynamics, leading to a transition from the stationary to oscillatory state. We propose a model where in the presence of AVB-B gap junctions, time-varying proprioceptive signals from the anterior body may easily induce changes in B-type motor neuron membrane potential, thus facilitating bending wave propagation.

A Nonlinear Model Recapitulates AVB-B Gap Junction-Dependent Bifurcation of B-Type Motor Neuron Dynamics. We next sought theoretical verification of our functional model. For simplicity, we developed a phenomenological model based on active Ca^{2+} and K^+ conductance (41), in which the dynamics of dorsal and ventral motor neurons within a given body segment are governed by the following equations:

$$\begin{cases} C_m\dfrac{dV_{di}}{dt} = -g_L(V_{di}-E_L) - g_{Ca}m_\infty(V_{di})*(V_{di}-E_{Ca}) \\ \qquad\qquad -g_K n_d*(V_{di}-E_K) + c'k_{i-1} + g(V_{AVB}-V_{di}), \\ \qquad\qquad \tau_n\dfrac{dn_d}{dt} = -n_d + n_\infty(V_{di}), \\ C_m\dfrac{dV_{vi}}{dt} = -g_L(V_{vi}-E_L) - g_{Ca}m_\infty(V_{vi})*(V_{vi}-E_{Ca}) \\ \qquad\qquad -g_K n_v*(V_{vi}-E_K) - c'k_{i-1} + g(V_{AVB}-V_{vi}), \\ \qquad\qquad \tau_n\dfrac{dn_v}{dt} = -n_v + n_\infty(V_{vi}). \end{cases} \quad [5]$$

In Eq. **5**, V is motor neuron membrane potential; subscripts d and v denote dorsal and ventral sides, respectively; m and n are voltage-dependent Ca^{2+} and K^+ activation variables, respectively. Parameter values in this equation were chosen (*Supporting Information*) to accommodate the following experimental findings. First, when the head and body undulations are decoupled ($c'k_1 \approx 0$), gap junctions between AVB interneurons and B-type motor neurons induce motor neuron oscillation (Fig. 5*A*). Second, proprioceptive signals arising from head bending entrain posterior motor neuron oscillation (Fig. 5*A*). The nullcline analysis, which allows for visualization of the dynamical variables on a vector field, provides useful information on the transition from the resting state to the limit cycle in the presence of AVB-B gap junctions (Fig. 5*B*). Furthermore, simulation recapitulated the experimental finding that AVB-B gap junctions help equalize bending amplitude along the body (Fig. 5*C*).

Electrical Couplings Between Motor Neurons and AVB-B Gap Junctions Permit Rapid and Reciprocal Interactions Between Head and Body Motor Activities. Having considered the functions of the descending interneuron inputs to B-type motor neurons, we next asked whether local gap junctions between motor neurons (Fig. 1*A*), which were suggested by electron microscopy analyses (25, 26), play roles in forward locomotion.

This question arises from the observation that optogenetic inhibition of B-type motor neurons in middle or posterior body regions, unlike the case of inhibiting the anterior body region, induced rapid (within ~300 ms) paralysis of the whole worm with the maximum laser intensity (Fig. 6 *A* and *B*, Fig. S6, and Movie S4). Electrical coupling is the best candidate for rapid redistribution of a hyperpolarization current among B-type motor neurons (P*acr-5*::Arch). In both *unc-7* mutants and AVB-ablated worms, whole-body paralysis could still be induced upon silencing midbody and posterior B-type motor neurons (Fig. 6*C*), using the maximum laser intensity, suggesting that the hyperpolarization signal could still be transduced in the absence of AVB-B gap junctions.

In *unc-9* mutants, however, rhythmic bending in the anterior body persisted when midbody B-type motor neurons were silenced (Fig. 6 *A* and *C* and Movie S5). Restoring UNC-9 expression in cholinergic motor neurons, including the B- and A-type motor neurons (P*acr-2*::UNC-9), restored the ability to optogenetically induce whole-body paralysis (Fig. 6*C*). Therefore, electrical couplings among motor neurons may contribute to the paralytic effect.

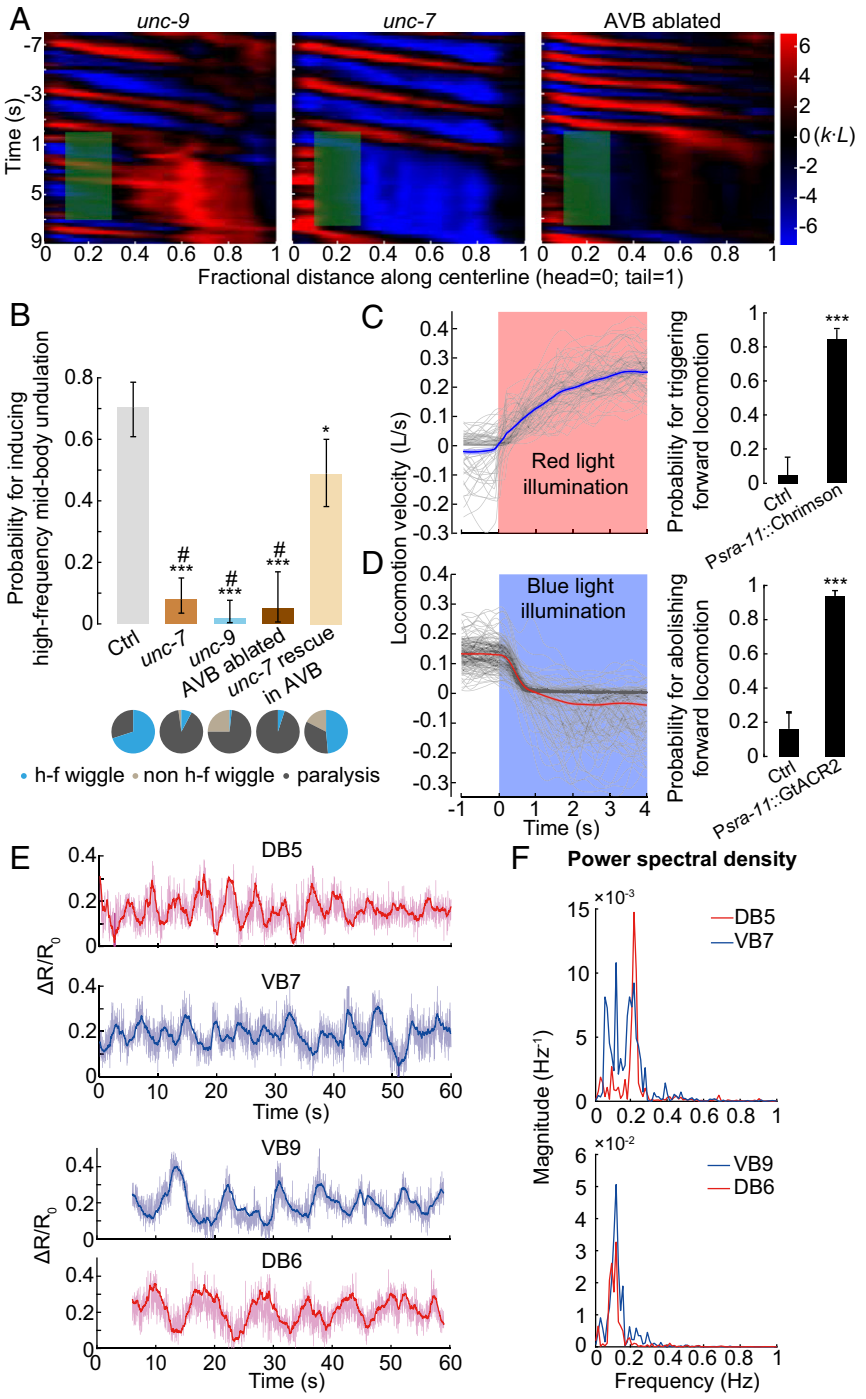

Fig. 4. AVB-B electrical coupling drives the bifurcation in the B-type neuron dynamics. (*A*) Representative curvature kymographs in AVB-B gap junction-deficient or AVB-ablated worms when anterior bending activity was abolished. (*B*) Probability for inducing high-frequency midbody undulation when anterior bending activity was abolished. Pie chart summarizes the percentage of worm locomotor states. Error bars indicate 95% binomial proportion confidence interval. ***$P < 0.0001$, *$P = 0.002$, #$P < 0.0001$ (*compared with Ctrl, #compared with UNC-7 rescued in AVB). χ^2 test. Strains for comparisons are as follows: control [P*acr-5*::Arch; P*unc-4*::TWK-18(gf)], $n = 113$ measurements, 13 worms; *unc-7* [*unc-7*(*hp121*); P*acr-5*::Arch; P*unc-4*::TWK-18(gf)], $n = 102$ measurements, 21 worms; *unc-9* [*unc-9*(*fc16*); P*acr-5*::Arch; P*unc-4*::TWK-18(gf)], $n = 116$ measurements, 26 worms; AVB-ablated [P*lgc-55(B)*::miniSOG, P*acr-5*::Arch], $n = 40$ measurements, 11 worms; UNC-7 rescued in AVB [*unc-7*(*hp121*); P*acr-5*::Arch; P*unc-4*::TWK-18(gf); P*sra-11*::UNC-7], $n = 86$ measurements, 12 worms. (*C*) Optogenetic activation of AVB premotor interneurons could trigger forward locomotion. (*Left*) Optogenetic activation (P*sra*-11::Chrimson, $n = 133$ measurements, 11 worms), showing locomotion velocity with time; red light (635 nm, 12 mW/mm^2) was turned on at $t = 0$. Gray traces represent individual trials, and shaded region represents SEM. (*Right*) Probability for triggering forward locomotion. (*D*) Optogenetic inhibition of AVB premotor interneurons could abolish forward locomotion. (*Left*) Optogenetic inhibition (P*sra-11*::GtACR2, $n = 187$ measurements, 21 worms), showing locomotion velocity with time; blue light (473 nm, 0.76 mW/mm^2) was turned on at $t = 0$. Gray traces represent individual trials, and shaded region represents SEM. (*Right*) Probability for abolishing forward locomotion. Ctrl represents worms without feeding ATR. Error bars indicate 95% binomial proportion confidence interval; ***$P < 0.0001$, χ^2 test. (*E*) Example traces of calcium dynamics of B-type motor neurons. Darker lines were smoothed data, using an exponential filter to reduce high-frequency noise. Upon light illumination that activated AVB interneurons, neighboring VB/DB motor neuron exhibited oscillatory yet anticorrelated calcium activities. To eliminate the proprioceptive coupling signal, we restrained the worm body region anterior to the imaging cells within a straight microfluidic channel. (*F*) Power spectral density of calcium dynamics using the smoothed data.

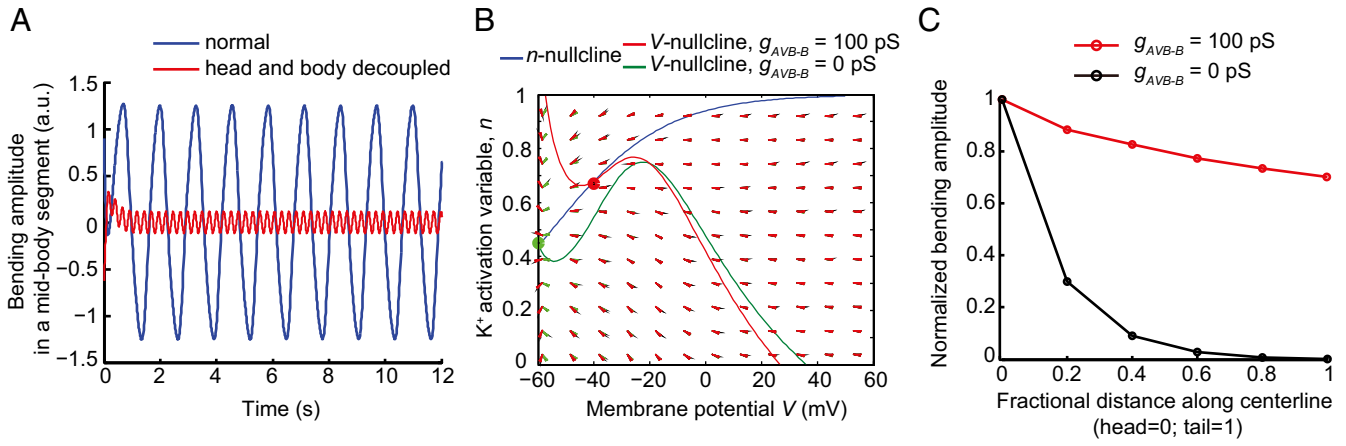

Fig. 5. Simulation of a nonlinear model. (*A*) Bending activity of a midbody segment. Blue, bending amplitude during normal locomotion; red, when the head and body undulation was decoupled, oscillation with higher frequency and lower amplitude emerged. (*B*) Nullcline analysis of motor neuron dynamics. The *n*- and *V*-nullclines were defined as $dn/dt = 0$, $dV/dt = 0$, respectively. In the absence of proprioceptive coupling and AVB-B gap junctions ($g_{AVB-B} = 0$), the fixed point of the membrane potential dynamics (green) corresponds to a steady state; in the presence of AVB-B gap junctions, that is, $g_{AVB-B} = 100$ ps, the system undergoes bifurcation, and the new fixed point becomes unstable (red), leading to periodic oscillation. (*C*) A comparison of bending amplitude along the body, with and without AVB-B gap junctions. All parameters used in the simulation are described in *Supporting Information*.

The efficacy for optogenetically inducing whole-body paralysis, however, was dose dependent. When the midbody B-type motor neurons were inactivated at lower laser intensity, which likely reduced the degree of hyperpolarization, forward locomotion was not abolished. Instead, both undulation amplitude and locomotor speed were reduced (Fig. 6 *D* and *E*). Interestingly, in the absence of AVB interneurons, a higher laser intensity was required to modify the locomotor kinematics, and to induce whole worm paralysis (Fig. 6 *D* and *E*). These results suggest a potential mechanism by which gap junctions between motor neurons and AVB-B gap junctions function together to retrogradely regulate head bending activity, and hence reconfigure the dynamics of worm body undulation.

Discussion

Electrical synapses are not only prevalent in invertebrate motor circuits, but also present in developing and mature vertebrate spinal cords (42–44). The functional implications of gap junctions in motor circuits and motor behaviors could be counterintuitive, confounding, and are often underappreciated (45, 46). In the mature zebrafish spinal cord, electrical couplings between motor neurons and premotor interneurons point to a potentially nimble feedback mechanism for modulating rhythmic activity (47). Experiments and modeling of crustacean stomatogastric ganglions suggest that the interplay between electrical and chemical synapses provides degenerate circuit mechanisms for switching between fast and slow oscillatory behaviors (48).

In the *C. elegans* motor circuit, the A-type motor neurons function as oscillators for reversal movements, and the descending AVA interneurons regulate their activities through a mixed gap junction and chemical synapse configuration (29, 49). At rest, AVA-A gap junctions shunt A-type motor neurons' intrinsic oscillatory activity so that a bias toward forward movement can be established (29, 49). Upon stimulation, the AVA interneurons potentiate A-type motor neuron oscillation mainly through chemical synaptic inputs (49), as well as gap junction-dependent antidromic rectification (50) that prolongs reversal movements.

In the motor circuit that drives *C. elegans* forward movement, we discovered that AVB-B electrical couplings induced oscillations in midbody B-type motor neurons and facilitated undulatory wave propagation. To better understand how descending inputs drove the bifurcation of motor neuron dynamics, we developed a nonlinear dynamic model based on voltage-dependent conductance. Detailed characterization of the intrinsic membrane conductance and experimental test of our model required electrophysiological recordings in motor neurons, a difficult technique that has only recently become possible (50). Intriguingly, a complementary study of the *C. elegans* reversal motor circuit found that P/Q/N-type voltage-dependent Ca^{2+} channels were required for generating intrinsic, oscillatory activity in the A-type motor neurons (49). Whether the same channels drive B-type motor neuron oscillation will be addressed in future studies.

Coordinated movement in larger animals involves networks of CPGs that are coupled through mechanosensory feedback (5). In leech, stretch-sensitive feedback can alter the intersegmental phase lags between CPGs (10, 51). During stick insect walking, proprioceptive feedback can entrain the motor patterns that drive individual joints, leading to interjoint coordination (13). Specific classes of mechanosensory neurons in fly larvae are required for efficient propagation of peristaltic waves (52, 53).

Here, our data indicate that distributed oscillators for forward movement, operated by at least some B-type motor neurons, exist in the *C. elegans* ventral nerve cord. Because worms must adapt to extreme ranges of external mechanical loads imposed by a changing environment (37), directional proprioceptive signals, also transduced by B-type motor neurons (31), are essential for entraining the rhythm of body oscillators, and for propagating coherent bending waves from the head to the tail (Fig. 7). In a linear coupling model where motor neurons passively respond to proprioceptive inputs, bending amplitude would suffer an exponential decay toward the tail. Our experimental finding and theoretical analysis thus provide insight into the interplay between sensory feedback and oscillators within the motor circuit.

We also found a previously unknown role of electrical couplings between motor neurons, which permits rapid and reciprocal interaction between the head and body motor activities (Figs. 6 and 7). Overexpression of UNC-9 in the B-type motor neurons led to constitutive paralysis (Movie S6); we suspect that strong electrical couplings between motor neurons tend to synchronize motor activity along the whole body, thus deteriorating bending wave propagation. Weak electrical couplings between motor neurons, on the other hand, may facilitate head bending activity and augment the excitability of motor neurons along the body. Direct testing of the functional contribution of local electrical couplings requires the elimination of electrical synapses between motor neurons, while sparing the AVB-B ones.

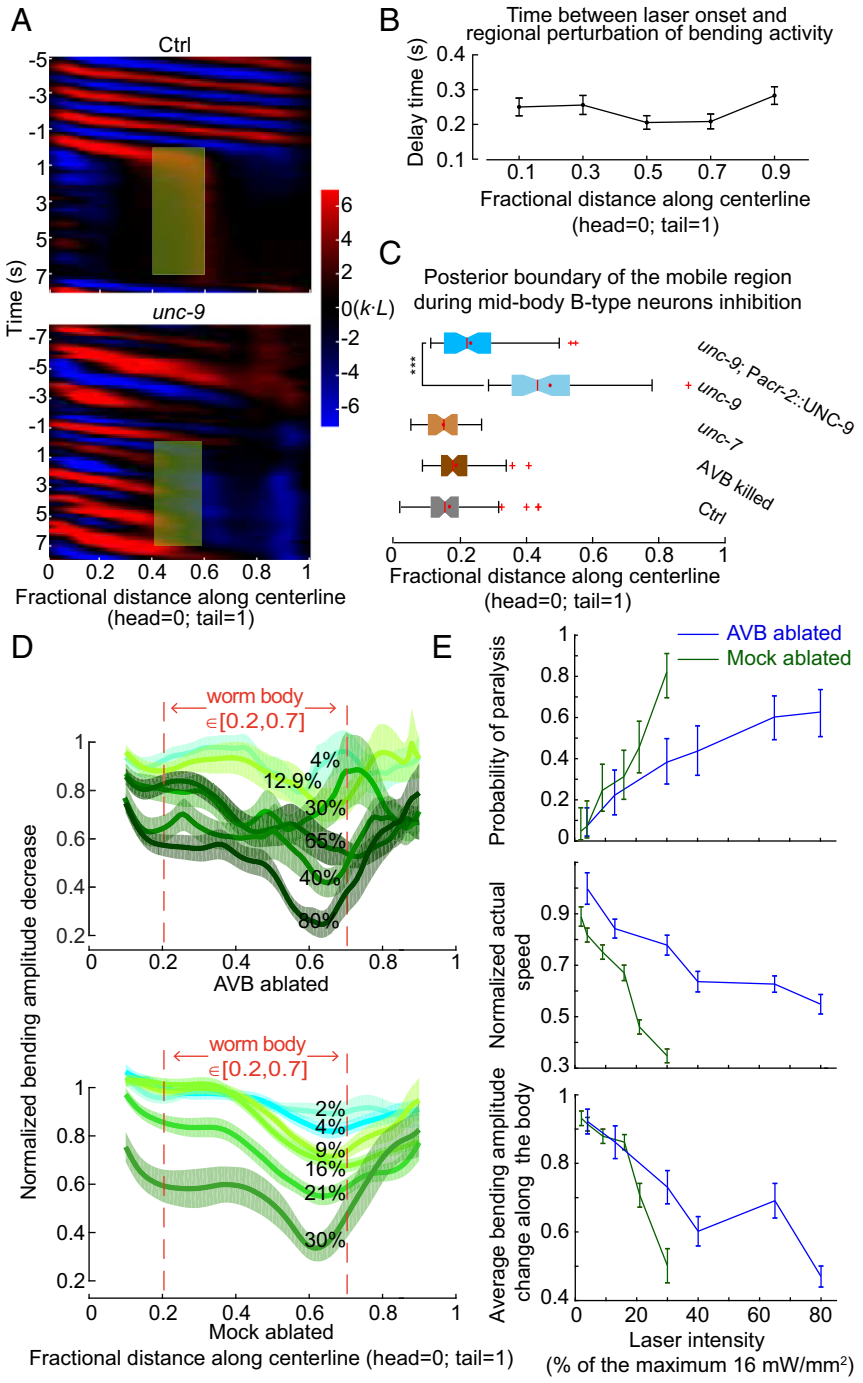

Fig. 6. Electrical coupling among motor neurons and AVB-B gap junctions allows for rapid and reciprocal interactions between head and body motor activities. (*A*) Comparison of representative curvature kymographs of control [P*acr-5*::Arch; P*unc-4*::TWK-18(gf)] and *unc-9* mutant [*unc-9*(*fc16*); P*acr-5*::Arch; P*unc-4*::TWK-18(gf)] worms during optogenetic inhibition of midbody B-type motor neurons. Green shaded regions are selected regions (0.4–0.6 fractional distance) subjected to 0- to 7-s stimulation by the green laser. (*B*) Delay time between the onset of green laser and changes in bending. Error bars are SEM (also see Fig. S6). (*C*) Quantification of the whole-body paralytic effect during optogenetic inhibition of midbody B-type motor neurons. Red crosses are outliers, red lines are medians, red dots are means, error bars represent Q1 − 1.5IQR and Q3 + 1.5IQR, respectively, and notches indicate 95% confidence interval. In *unc-9* mutants, the boundary shifted toward the midbody, reflecting that the anterior body could still undulate. ***$P < 0.0001$, Mann–Whitney *U* test. Control [P*acr-5*::Arch; P*unc-4*::TWK-18(gf)], $n = 70$ measurements, 17 worms; *unc-7* [*unc-7*(*hp121*); P*acr-5*::Arch; P*unc-4*::TWK-18(gf)], $n = 43$ measurements, 11 worms; *unc-9* [*unc-9*(*fc16*); P*acr-5*::Arch; P*unc-4*::TWK-18(gf)], $n = 59$ measurements, 17 worms; AVB-ablated (P*lgc-55*::miniSOG, P*acr-5*::Arch), $n = 65$ measurements, 18 worms; UNC-9 rescued in the B-type and A-type motor neurons [*unc-9*(*fc16*); P*acr-5*::Arch; P*acr-2*::UNC-9], $n = 48$ measurements, 9 worms. (*D*) Laser intensity-dependent effects on the bending amplitude along the body. Error bars are SEM. (*E*) Laser intensity-dependent effects on efficacy for inducing whole-body paralysis, locomotion speed and mean amplitude decreases along the body [0.2, 0.7]. Error bars (speed and amplitude) are SEM; error bars (paralysis) are 95% binomial proportion confidence intervals. $n \geq 42$ measurements, ≥6 worms for each data point. Maximum laser intensity, 16 mW/mm^2.

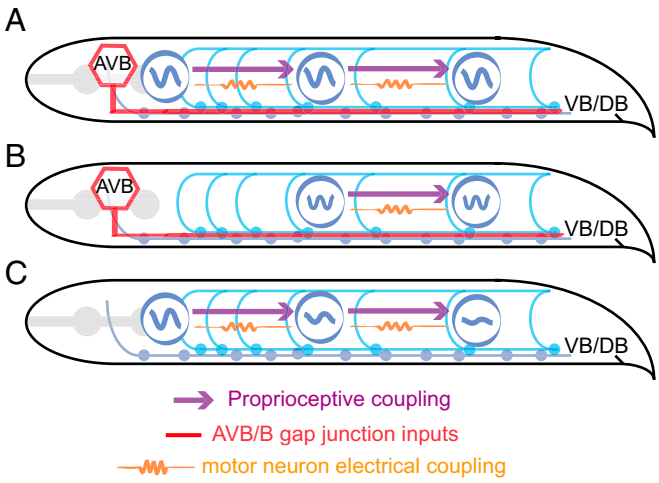

Fig. 7. Model schematics of coordinating forward locomotion in *C. elegans*. (*A*) Proprioceptive coupling between B-type motor neurons, AVB-B gap junction coupling, and weak electrical coupling between motor neurons work synergistically to drive and propagate a coordinated undulatory wave from the head to the tail. (*B*) When a strong and time-varying proprioceptive signal from an anterior body region is absent, AVB-B gap junction coupling induces midbody high-frequency undulation. (*C*) In the absence of AVB-B gap junction inputs, proprioceptive couplings are less effective in propagating bending waves, leading to rapidly decaying bending amplitude toward the tail.

Current genetic tools for manipulating gap junction expression with defined wiring specificity remain to be developed because both types of gap junctions require UNC-9 innexin.

UNC-9 is also expressed by the body wall muscle cells (54). Could electrical couplings between muscle cells and those between motor neurons have similar functions? We (and others) found that optogenetic inhibition of midbody muscle cells did not affect bending activity in the anterior body, but did abolish bending activity in the posterior body (55). This effect is consistent with our proprioceptive coupling model (Fig. 7). Furthermore, in *unc-13* mutants, where all chemical synaptic inputs from motor neurons to muscles are eliminated, targeted optogenetic activation of ventral or dorsal muscle cells induces local body bending, not bending in neighboring regions (31). These data suggest that any electrical coupling between body wall muscle cells only plays a restricted role for *C. elegans* body bend propagation.

Despite substantial anatomical differences between the worm motor circuit and those in higher organisms, we identified converging principles that govern coordinated locomotion. By integrating global descending signals, biomechanical feedback, and neuromuscular dynamics, our findings and models represent a key step toward a full system model of animal locomotion.

Methods

Worm Strains and Cultivation. Wild-type (N2), mutant, and transgenic worms were cultivated using standard methods (56). Strain information can be found in Table S1. Transgenic worms used in all optogenetic experiments were cultivated in the dark at 20–25 °C on NGM plates with *Escherichia coli* OP50 and all-*trans* retinal (ATR). We performed all experiments using young adult hermaphrodites.

Microfluidic Device. Custom microfluidic devices were fabricated in polydimethylsiloxane using soft lithography. We loaded each microfluidic channel with dextran solution [~25% (wt/wt) dextran in M9 buffer (1 Pa·s viscosity)]. An individual worm was transferred into the inlet of each microfluidic channel, and worm position within each channel was manually controlled by syringes connected to polyethylene tubing.

Behavioral Quantification and Optogenetic Manipulation. Experiments were performed on a Nikon inverted microscope (Ti-U) under 10× magnification with dark-field illumination. Worms were immersed in viscous solution [~25% (wt/wt) dextran in M9 buffer in most cases], sandwiched between two glass slides, and retained within the field of view of an imaging objective by a custom tracking system. Video sequences were taken by a Basler CMOS camera (aca2000-340km), and the worm body centerline was extracted in real time. We used MATLAB custom software (MathWorks) for postprocessing behavioral data. We used the CoLBeRT system (55) to perform spatially selective optogenetic manipulation for different motor circuit components. For optogenetic inhibition, we used a 561-nm solid-state laser with maximum intensity at 16 mW/mm^2 (Arch) or a 473-nm solid-state laser at 0.76 mW/mm^2 (GtACR2).

In the relevant figure legends, the *n* numbers, in most cases, denote the numbers of measurements on indicated numbers of different animals for the experiments and represent both independent biological replication and technical replication.

Optogenetic Ablation. Optogenetic ablation was carried out using transgenic strains, in which miniSOG was specifically expressed in *C. elegans* neurons. We used mitochondrially targeted miniSOG (TOMM20-miniSOG) (34) and a membrane-targeted miniSOG (PH-miniSOG) (57) to induce cell death in cell-autonomous manner upon blue light stimulation. We used miniSOG to ablate multiple neurons that include AVB [*Plgc*-55(B)::tomm-20-miniSOG]. L2/early L3 worms cultivated on OP50 were transplanted to an unseeded NGM plate, restricted within a 1.7-cm^2 area via filter paper with a hole in the center and soaked with 100 μM $CuCl_2$. Worms were illuminated with blue LED (M470L3-C5; Thorlabs) with an intensity of 80.2 mW/cm^2, measured by a power meter (PM16-130; Thorlabs). The temporal sequence was 0.5/1.5 s on/off pulses for 30 min. Mock ablations were performed via green light illumination using the same genotype under otherwise identical experimental conditions.

To ablate only AVB interneurons, we used a transgenic strain carrying PH-miniSOG [P*sra-11*::PH-miniSOG]. L2/early L3 worm cultivated on OP50 was transplanted to 3% (wt/vol) agarose-coated glass slide and was covered with a cover glass to constrain worm motion. Guided by fluorescence signal, somas and axons of AVB interneurons were targeted and illuminated with 76 mW/cm^2 intensity blue laser for 2 min under 20× objective using custom single-neuron–targeting CoLBeRT system. After illumination, worms were transplanted to OP50-seeded NGM plates with/without ATR for behavioral experiments.

For selective B-type motor neuron ablation (*Pacr-5*::TOMM20-miniSOG), single L3 worms were transferred from the OP50-seeded NGM plates to 3% agarose-coated glass slides. The worms were covered by a cover glass to remain stationary. Spatially selective illumination patterns were generated by a digital micromirror device (DLI4130 0.7 XGA; Digital Light Innovations) to target individual neurons through a 20× objective mounted on a Nikon inverted microscope (Ti-U). Neurons were identified using mCherry fluorescence signals. We used a 473-nm blue laser with an intensity of 29 mW/mm^2. The temporal sequence was 0.5/1.5 s on/off pulses for 15 min. After illumination, the worms were recovered by 2 μL of M9 buffer, and then transferred to OP50-seeded NGM plates with/without ATR for behavioral experiments.

Calcium Imaging and Optogenetic Stimulation. We imaged the B-type motor neurons in *unc-13* mutants using wide-field fluorescent microscopy. Anterior body region of a single young adult worm was restrained in a straight microfluidic channel; middle and posterior body regions were freely immersed in liquid solution (5% dextran). *hpIs458*, an integrated calcium reporter transgene that expresses the GCaMP6s::wCherry fusion protein in the B-type motor neurons, was excited by blue and yellow light. Green and red fluorescence emission signals were collected through a Nikon Plan Apo 20× objective (working distance, 1 mm; N.A., 0.75), separated and relayed (Andor Optosplit), and projected simultaneously onto one-half of sCMOS sensor (Andor Zyla 4.2). Motor neurons of interest were automatically identified using custom-written MATLAB scripts, and the calcium dynamics were calculated as the ratio of GCaMP6 to wCherry fluorescence emission intensities. Calcium imaging and optogenetic stimulation of head interneurons including AVB (green light) were synchronized. Worms without feeding ATR were used as control, while other experimental conditions remained identical.

Note. Two related works [Gao et al. (49) and Fouad et al. (58)] on the backward and forward motor circuit of *C. elegans* were in print when this work was under review. An earlier version of this work can be found at https://www.biorxiv.org/content/early/2017/06/18/131490.

ACKNOWLEDGMENTS. We thank Christopher Fang-Yen and Anthony Fouad for discussions. We also thank two anonymous reviewers for their critical comments. This work was funded by the Chinese Academy of Sciences Hundred Talents Plan and National Science Foundation of China Grants NSFC-31471051 and NSFC-91632102 (to Q.W.) and Canadian Institute of Health Research Grants CIHR-MOP93619 and MOP123250 (to M.Z.).

1. Brown TG (1911) The intrinsic factors in the act of progression in the mammal. *Proc R Soc Lond B Biol Sci* 84:308–319.
2. Delcomyn F (1980) Neural basis of rhythmic behavior in animals. *Science* 210:492–498.
3. Grillner S (2003) The motor infrastructure: From ion channels to neuronal networks. *Nat Rev Neurosci* 4:573–586.
4. Kiehn O (2006) Locomotor circuits in the mammalian spinal cord. *Annu Rev Neurosci* 29:279–306.
5. Marder E, Bucher D, Schulz DJ, Taylor AL (2005) Invertebrate central pattern generation moves along. *Curr Biol* 15:R685–R699.
6. Marder E, Calabrese RL (1996) Principles of rhythmic motor pattern generation. *Physiol Rev* 76:687–717.
7. Mullins OJ, Hackett JT, Buchanan JT, Friesen WO (2011) Neuronal control of swimming behavior: Comparison of vertebrate and invertebrate model systems. *Prog Neurobiol* 93:244–269.
8. Pearson KG (1995) Proprioceptive regulation of locomotion. *Curr Opin Neurobiol* 5: 786–791.
9. McClellan AD, Jang W (1993) Mechanosensory inputs to the central pattern generators for locomotion in the lamprey spinal cord: Resetting, entrainment, and computer modeling. *J Neurophysiol* 70:2442–2454.
10. Yu X, Friesen WO (2004) Entrainment of leech swimming activity by the ventral stretch receptor. *J Comp Physiol A Neuroethol Sens Neural Behav Physiol* 190:939–949.
11. Pearson KG (2004) Generating the walking gait: Role of sensory feedback. *Prog Brain Res* 143:123–129.
12. Akay T, Tourtellotte WG, Arber S, Jessell TM (2014) Degradation of mouse locomotor pattern in the absence of proprioceptive sensory feedback. *Proc Natl Acad Sci USA* 111:16877–16882.
13. Hess D, Büschges A (1999) Role of proprioceptive signals from an insect femur-tibia joint in patterning motoneuronal activity of an adjacent leg joint. *J Neurophysiol* 81: 1856–1865.
14. Woo SH, et al. (2015) Piezo2 is the principal mechanotransduction channel for proprioception. *Nat Neurosci* 18:1756–1762.
15. Lemon RN (2008) Descending pathways in motor control. *Annu Rev Neurosci* 31: 195–218.
16. Hägglund M, Borgius L, Dougherty KJ, Kiehn O (2010) Activation of groups of excitatory neurons in the mammalian spinal cord or hindbrain evokes locomotion. *Nat Neurosci* 13:246–252.
17. Thiele TR, Donovan JC, Baier H (2014) Descending control of swim posture by a midbrain nucleus in zebrafish. *Neuron* 83:679–691.
18. Severi KE, et al. (2014) Neural control and modulation of swimming speed in the larval zebrafish. *Neuron* 83:692–707.
19. Buchanan JT, Brodin L, Dale N, Grillner S (1987) Reticulospinal neurones activate excitatory amino acid receptors. *Brain Res* 408:321–325.
20. Bouvier J, et al. (2015) Descending command neurons in the brainstem that halt locomotion. *Cell* 163:1191–1203.
21. Esposito MS, Capelli P, Arber S (2014) Brainstem nucleus MdV mediates skilled forelimb motor tasks. *Nature* 508:351–356.
22. Weeks JC, Kristan WB (1978) Initiation, maintenance and modulation of swimming in the medicinal leech by the activity of a single neuron. *J Exp Biol* 77:71–88.
23. Friesen WO, Kristan WB (2007) Leech locomotion: Swimming, crawling, and decisions. *Curr Opin Neurobiol* 17:704–711.
24. Dickinson MH, et al. (2000) How animals move: An integrative view. *Science* 288: 100–106.
25. Chen BL, Hall DH, Chklovskii DB (2006) Wiring optimization can relate neuronal structure and function. *Proc Natl Acad Sci USA* 103:4723–4728.
26. White JG, Southgate E, Thomson JN, Brenner S (1986) The structure of the nervous system of the nematode *Caenorhabditis elegans*. *Philos Trans R Soc Lond B Biol Sci* 314:1–340.
27. White JG, Southgate E, Thomson JN, Brenner S (1976) The structure of the ventral nerve cord of *Caenorhabditis elegans*. *Philos Trans R Soc Lond B Biol Sci* 275:327–348.
28. Starich TA, Xu J, Skerrett IM, Nicholson BJ, Shaw JE (2009) Interactions between innexins UNC-7 and UNC-9 mediate electrical synapse specificity in the *Caenorhabditis elegans* locomotory nervous system. *Neural Dev* 4:16.
29. Kawano T, et al. (2011) An imbalancing act: Gap junctions reduce the backward motor circuit activity to bias *C. elegans* for forward locomotion. *Neuron* 72:572–586.
30. Chalfie M, et al. (1985) The neural circuit for touch sensitivity in *Caenorhabditis elegans*. *J Neurosci* 5:956–964.
31. Wen Q, et al. (2012) Proprioceptive coupling within motor neurons drives *C. elegans* forward locomotion. *Neuron* 76:750–761.
32. Zhen M, Samuel AD (2015) *C. elegans* locomotion: Small circuits, complex functions. *Curr Opin Neurobiol* 33:117–126.
33. Altun ZF, Chen B, Wang ZW, Hall DH (2015) High resolution map of *Caenorhabditis elegans* gap junction proteins. *Dev Dyn* 244:903.
34. Qi YB, Garren EJ, Shu X, Tsien RY, Jin Y (2012) Photo-inducible cell ablation in *Caenorhabditis elegans* using the genetically encoded singlet oxygen generating protein miniSOG. *Proc Natl Acad Sci USA* 109:7499–7504.
35. Faumont S, et al. (2011) An image-free opto-mechanical system for creating virtual environments and imaging neuronal activity in freely moving *Caenorhabditis elegans*. *PLoS One* 6:e24666.
36. Laurent P, et al. (2015) Decoding a neural circuit controlling global animal state in *C. elegans*. *eLife* 4:e04241.
37. Fang-Yen C, et al. (2010) Biomechanical analysis of gait adaptation in the nematode *Caenorhabditis elegans*. *Proc Natl Acad Sci USA* 107:20323–20328.
38. Backholm M, Ryu WS, Dalnoki-Veress K (2013) Viscoelastic properties of the nematode *Caenorhabditis elegans*, a self-similar, shear-thinning worm. *Proc Natl Acad Sci USA* 110:4528–4533.
39. Ermentrout GB, Kopell N (1984) Frequency plateaus in a chain of weakly coupled oscillators. 1. *SIAM J Math Anal* 15:215–237.
40. Govorunova EG, Sineshchekov OA, Janz R, Liu X, Spudich JL (2015) NEUROSCIENCE. Natural light-gated anion channels: A family of microbial rhodopsins for advanced optogenetics. *Science* 349:647–650.
41. Izhikevich EM (2007) *Dynamical Systems in Neuroscience: The Geometry of Excitability and Bursting* (MIT Press, Cambridge, MA).
42. Connors BW, Long MA (2004) Electrical synapses in the mammalian brain. *Annu Rev Neurosci* 27:393–418.
43. Kiehn O, Tresch MC (2002) Gap junctions and motor behavior. *Trends Neurosci* 25: 108–115.
44. Szczupak L (2016) Functional contributions of electrical synapses in sensory and motor networks. *Curr Opin Neurobiol* 41:99–105.
45. Manor Y, Rinzel J, Segev I, Yarom Y (1997) Low-amplitude oscillations in the inferior olive: A model based on electrical coupling of neurons with heterogeneous channel densities. *J Neurophysiol* 77:2736–2752.
46. Marder E (1998) Electrical synapses: Beyond speed and synchrony to computation. *Curr Biol* 8:R795–R797.
47. Song J, Ampatzis K, Björnfors ER, El Manira A (2016) Motor neurons control locomotor circuit function retrogradely via gap junctions. *Nature* 529:399–402.
48. Gutierrez GJ, O'Leary T, Marder E (2013) Multiple mechanisms switch an electrically coupled, synaptically inhibited neuron between competing rhythmic oscillators. *Neuron* 77:845–858.
49. Gao S, et al. (2018) Excitatory motor neurons are local oscillators for backward locomotion. *eLife* 7:e29915.
50. Liu P, Chen B, Mailler R, Wang ZW (2017) Antidromic-rectifying gap junctions amplify chemical transmission at functionally mixed electrical-chemical synapses. *Nat Commun* 8:14818.
51. Yu X, Nguyen B, Friesen WO (1999) Sensory feedback can coordinate the swimming activity of the leech. *J Neurosci* 19:4634–4643.
52. Cheng LE, Song W, Looger LL, Jan LY, Jan YN (2010) The role of the TRP channel NompC in *Drosophila* larval and adult locomotion. *Neuron* 67:373–380.
53. Guo Y, et al. (2016) Transmembrane channel-like (tmc) gene regulates *Drosophila* larval locomotion. *Proc Natl Acad Sci USA* 113:7243–7248.
54. Liu Q, Chen B, Gaier E, Joshi J, Wang ZW (2006) Low conductance gap junctions mediate specific electrical coupling in body-wall muscle cells of *Caenorhabditis elegans*. *J Biol Chem* 281:7881–7889.
55. Leifer AM, Fang-Yen C, Gershow M, Alkema MJ, Samuel AD (2011) Optogenetic manipulation of neural activity in freely moving *Caenorhabditis elegans*. *Nat Methods* 8:147–152.
56. Brenner S (1974) The genetics of *Caenorhabditis elegans*. *Genetics* 77:71–94.
57. Xu S, Chisholm AD (2016) Highly efficient optogenetic cell ablation in *C. elegans* using membrane-targeted miniSOG. *Sci Rep* 6:21271.
58. Fouad, et al. (2018) Distributed rhythm generators underlie *Caenorhabditis elegans* forward locomotion. *eLife* 7:e29913.